

# Hydrogen-doped viscoplastic liquid metal microparticles for stretchable printed metal lines

Selvaraj Veerapandian<sup>1,7</sup>, Woosun Jang<sup>1,2,5,7</sup>, Jae Bok Seo<sup>3,6</sup>, Hongbo Wang<sup>1,4</sup>, Minsik Kong<sup>1</sup>, Kaliannan Thiagarajan<sup>1</sup>, Junghyeok Kwak<sup>1</sup>, Gyeongbae Park<sup>1</sup>, Gilwoon Lee<sup>1</sup>, Wonjeong Suh<sup>1,4</sup>, Insang You<sup>1</sup>, Mehmet Emin Kılıç<sup>2</sup>, Anupam Giri<sup>1</sup>, Lucia Beccai<sup>4</sup>, Aloysius Soon<sup>1,2</sup> and Unyong Jeong<sup>1</sup>

**Conductive and stretchable electrodes that can be printed directly on a stretchable substrate have drawn extensive attention for wearable electronics and electronic skins. Printable inks that contain liquid metal are strong candidates for these applications, but the insulating oxide skin that forms around the liquid metal particles limits their conductivity. This study reveals that hydrogen doping introduced by ultrasonication in the presence of aliphatic polymers makes the oxide skin highly conductive and deformable. X-ray photoelectron spectroscopy and atom probe tomography confirmed the hydrogen doping, and first-principles calculations were used to rationalize the obtained conductivity. The printed circuit lines show a metallic conductivity ( $25,000 \text{ S cm}^{-1}$ ), excellent electromechanical decoupling at a 500% uniaxial stretching, mechanical resistance to scratches and long-term stability in wide ranges of temperature and humidity. The self-passivation of the printed lines allows the direct printing of three-dimensional circuit lines and double-layer planar coils that are used as stretchable inductive strain sensors.**

Stretchable electronic devices have received widespread attention for potential uses in healthcare monitoring<sup>1–3</sup>, electronic skins<sup>4,5</sup> and wearable haptic devices<sup>6,7</sup>. One of the key technological issues in stretchable electronics is the fabrication of stretchable circuit lines, for which several characteristics are required simultaneously—metallic conductivity, negligible resistance changes under deformations, electrical stability in harsh environments, printing of complicated circuit designs, passivation<sup>8</sup> and good adhesion to elastomeric substrates<sup>9</sup>. Serpentine and buckled metal interconnections have achieved a few of the above requirements, such as metallic conductivity, small resistance changes and some degree of deformability, as well as environmental stability<sup>10</sup>. Other progress has been with conductive elastomer composites with respect to high stretchability, printability and environmental stability<sup>11,12</sup>. Despite the many efforts so far, the fabrication of deformable circuit lines still needs notable progress.

In recent years, liquid metals (LMs, such as eutectic alloys of Ga and In) have been explored as an alternative to solid metal conductors because of their extreme stretchability and metallic conductivity ( $34,000 \text{ S cm}^{-1}$ ) (refs. <sup>7,13,14</sup>). LM microparticles (MPs) were used to fabricate circuit lines on latex gloves<sup>15</sup> and as an additive to a silver flake composite<sup>16</sup>. Unfortunately, as LM MPs are non-conductive due to the oxide skin<sup>17,18</sup>, electrical conduction was activated after removing the oxide skin by chemical etching<sup>19</sup> or mechanical scratching<sup>18</sup>. Alloying with other metals (Mg, Cu and Fe) was suggested as a possible way to remove oxides<sup>20–23</sup>; however, the alloy had a low electrical conductivity ( $2,000 \text{ S cm}^{-1}$ ) and its brittleness caused unstable conductance under stretching. To take full advantage of

LMs, the oxide skin should be highly conductive and deformable. In this study, through experimental characterization and theoretical calculations, we report that hydrogen doping (H-doping) can create a highly conductive viscoplastic oxide skin on the LM MPs. We used the LM MPs solution as an ink to print circuit lines that can meet the demands of ideal stretchable circuit lines, and we demonstrate a high-performance stretchable inductive strain sensor with a double-layer coil.

H-doped MPs were reproduced by applying ultrasonication to a solution that contained toluene, bulk LM, poly(ethylene-co-vinylacetate) (PEVA) and a free radical initiator (dicumyl peroxide, DCP) (Fig. 1a). Ultrasonication caused elongation and breaking of the bulk LM and created MPs due to the large surface tension<sup>24</sup>. The primary carbon radicals ( $\sim\text{C}-\text{C}\cdot$ ) were generated from the aliphatic segments in PEVA<sup>25</sup>. The radicals generated from DCP were transferred to PEVA and produce secondary carbon radicals ( $\sim\text{C}-\text{C}-\text{C}\cdot$ ) (ref. <sup>26</sup>) that underwent  $\beta$  scission to yield primary carbon radicals<sup>27</sup>. The primary carbon radicals yielded hydrogen radicals ( $\text{H}\cdot$ ) (ref. <sup>27</sup>), which donated electrons to oxygen and existed in the protonated state ( $\text{M}-\text{O}^2-\text{H}^+$ ) (ref. <sup>28</sup>). The details are found in Methods and Supplementary Fig. 1 and the accompanying text.

Figure 1b,c exhibits the X-ray photoelectron spectroscopy (XPS) spectra (O 1s, Ga 3d and In 3d) of the undoped MPs prepared in pure toluene (Fig. 1b) and the H-doped MPs obtained after washing the polymer in pure solvent (Fig. 1c). In addition, atom probe tomography (APT) was performed for the two MPs. Detailed elemental analysis is provided in Supplementary Figs 2–5, Supplementary Table 1 and the accompanying text. From the O 1s

<sup>1</sup>Department of Materials Science and Engineering, Pohang University of Science and Technology, Pohang, Korea. <sup>2</sup>Department of Material Science and Engineering and Center for Artificial Synesthesia Materials Discovery, Yonsei University, Seoul, Korea. <sup>3</sup>National Institute for Nanomaterials Technology, Pohang University of Science and Technology, Pohang, Korea. <sup>4</sup>Center for Micro-BioRobotics (CMBR@SSSA), Istituto Italiano di Tecnologia, Pontedera, Italy. <sup>5</sup>Present address: Department of Inorganic Chemistry, Fritz-Haber Institute of the Max-Planck Society, Berlin, Germany. <sup>6</sup>Present address: Department of Materials Engineering and Convergence Technology, Center for K-metal, Gyeongsang National University (GNU), Jinju, South Korea. <sup>7</sup>These authors contributed equally: Selvaraj Veerapandian, Woosun Jang. <sup>✉</sup>E-mail: [aloysius.soon@yonsei.ac.kr](mailto:aloysius.soon@yonsei.ac.kr); [ujeong@postech.ac.kr](mailto:ujeong@postech.ac.kr)

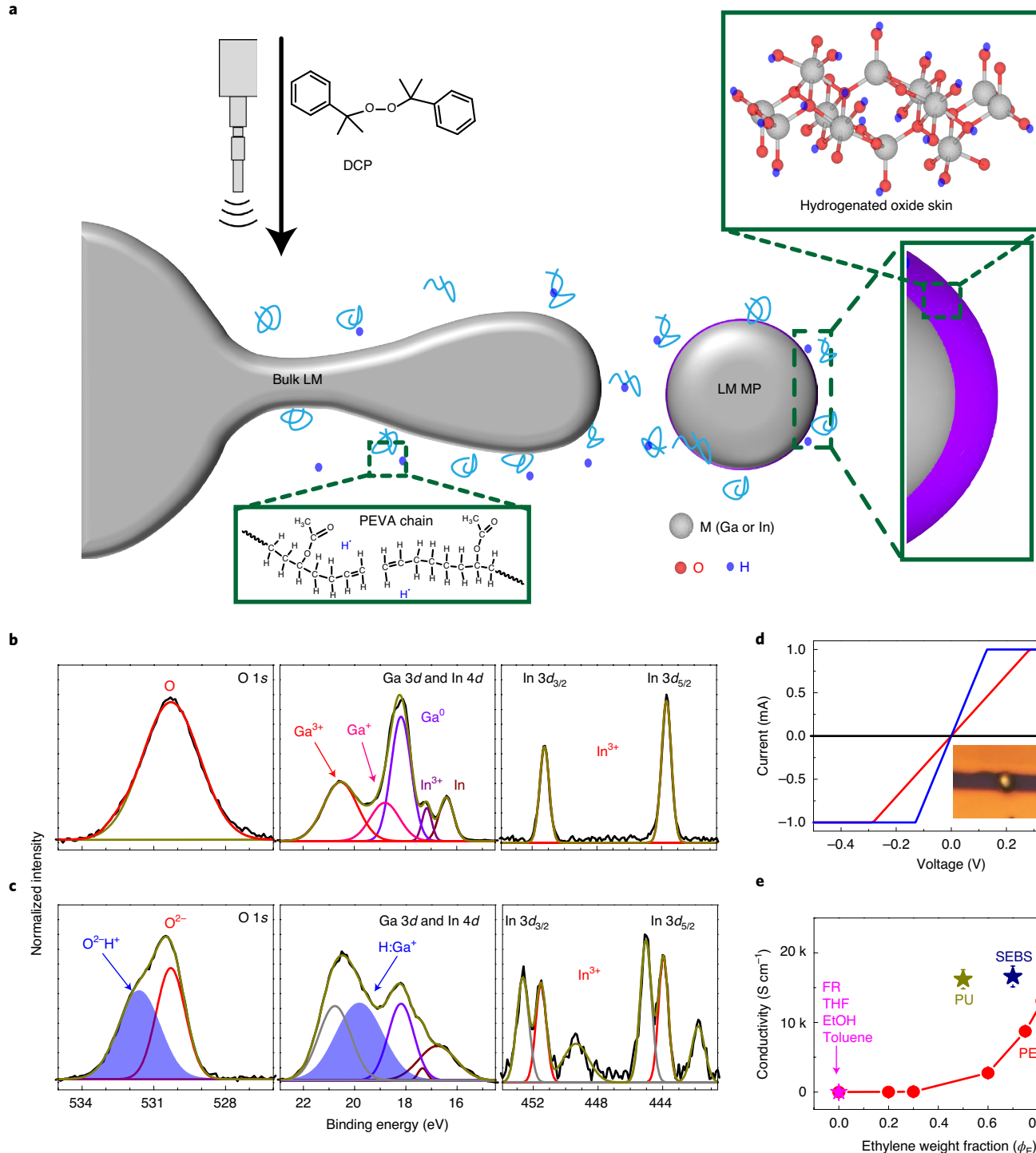


**Fig. 1 | Characterization of the H-doped LM MPs.** **a**, Hydrogen radical formation from the alkyl-containing block of PEVA by ultrasonication in the presence of a radical initiator (DCP) and the subsequent H-doping in the oxide skin. **b,c**, XPS of O 1s, Ga 3d and In 3d of the undoped MPs (**b**) and the H-doped MPs (**c**). The deconvoluted curves (green) in **c** indicate the contribution by H-doping. **d**, Comparison of the I–V curves obtained from a single MP produced at different conditions. Inset: OM image of a single MP located between two Au lines. The MPs prepared with PEVA (with or without DCP (blue and red lines, respectively)) were highly conductive; however, the undoped MP prepared without PEVA (black line) was insulating. **e**, Conductivities of the printed lines according to  $\phi_E$  in PEVA (red line). The MPs prepared in pure solvents (ethanol, toluene and THF) were not conductive. The MPs with polymers of  $\phi_E=0$  (FR and Ecoflex) were insulating, whereas the MPs with polymers of a large  $\phi_E$  (PU and SEBS) were conductive.

spectrum, most of the oxygen of the undoped MPs existed in the oxide state<sup>29</sup>; however, oxygen in the H-doped MPs showed a broad additional peak (531.7 eV), which corresponded to  $\text{O}^{2-}$  from the  $-\text{M(OH)}_x$  at the surface and  $\text{M-O}^{2-}\text{H}^+$  in the oxide<sup>28,30</sup>. In the Ga

3d spectrum of the H-doped MPs, the H-doping contribution ( $\text{Ga-O}^{2-}\text{H}^+$ , 19.8 eV) (ref. <sup>31</sup>) was notable in the broad peak (19–22 eV), which corresponded to the hydroxide formation<sup>31,32</sup> ( $\text{Ga}^+$ ,  $\text{Ga}^{3+}$  and  $\text{In}^{3+}$ ). In the In 3d spectrum of the H-doped MPs, additional peaks

for  $\text{In(OH)}_x$  appeared at 445 eV and 452.6 eV (ref. <sup>33</sup>). From the XPS results, the fraction of oxygen in the H-doped state ( $\text{M}-\text{O}^2-\text{H}^+$ ) in the oxide layer was 15.8%, and thus the concentration of  $\text{H}^+$  was 7.0 at%. In the APT measurements and the C 1s XPS spectrum (289.1 eV), surface adsorption of a small amount of PEVA on the H-doped MPs was confirmed.

It is well-known that metal nanowires stabilized by polymers are conductive unless a continuous polymer coating is formed on the surface<sup>34</sup>. Figure 1d shows the current–voltage ( $I-V$ ) curves of a single MP located between patterned Au lines. The MP prepared with both PEVA and DCP was the most conductive, the MP made only with PEVA was less so, but still highly conductive, and the undoped MP prepared in pure toluene was insulating. These results indicate that the H-doped oxide is conductive without a polymer coating layer (Supplementary Fig. 6) and the H<sup>+</sup> formation was accelerated by DCP. The conductivity of Ga- or In-based alloys is dependent on the extent of H-doping<sup>28,35,36</sup>. As H<sup>+</sup> generation is proportional to the ethylene weight fraction ( $\phi_E$ ) in PEVA, the conductivity increased as  $\phi_E$  increased (red line in Fig. 1e). The printed lines of the MPs prepared in pure ethanol or toluene were insulating, and the lines with the MPs prepared in tetrahydrofuran (THF) showed a low conductivity ( $1.0 \text{ S cm}^{-1}$ ). The highest conductivity ( $\sigma=25,000 \text{ S cm}^{-1}$ ) was obtained with PEVA-88 ( $\phi_E=0.88$ ) and the addition of DCP (Supplementary Table 2). We used these in further experiments.

In addition, we investigated the  $\phi_E$  effect with other polymers, which included fluorinated silicone rubber (FR,  $\phi_E=0$ ), poly(vinyl acetate) ( $\phi_E=0$ ), poly(vinyl alcohol) ( $\phi_E=0$ ), polyurethane (PU,  $\phi_E=0.5$ ) and polystyrene-b-poly(ethylene butylene)-b-polystyrene (SEBS,  $\phi_E=0.7$ ). The MPs produced in the polymers with  $\phi_E=0$  were insulating, whereas the MPs prepared in PU and SEBS had a similar conductivity to those prepared in PEVA ( $\phi_E=0.82-0.88$ ). Increasing  $\phi_E$  enhanced both the modulus and conductivity of the composite (Supplementary Fig. 7); however, the conductivity was not related to the modulus. Although FR, Ecoflex and PEVA ( $\phi_E=0.6$ ) had a similar modulus (~3 MPa), only PEVA produced conductive MPs. It is notable that effective H-doping took place only under ultrasonication. When the premade undoped MPs were provided with radicals by annealing the PEVA/DCP solution at 200 °C, they were insulating, but became conductive after ultrasonication.

Many works reported an amorphous state of the LM oxide layer, and we could not observe X-ray diffraction peaks from the MPs (Supplementary Fig. 8), whereas crystalline indium gallium oxide thin films have been reported<sup>37</sup>. Thus, we investigated the effect of H-doping in both amorphous and crystalline states of the oxide skin by first principles density functional theory (DFT) calculations using metal–oxygen structural motifs found in pristine  $\text{In}_2\text{O}_3$  (cubic lattice) and  $\text{Ga}_2\text{O}_3$  (monoclinic lattice) (Fig. 2a and Supplementary Fig. 9). Figure 2b exhibits the atomic structures of  $(\text{In}_{0.5}\text{Ga}_{0.5})_2\text{O}_3$  as an example, which has 1.23 at% of H-doped oxide and a 50:50 In-to-Ga ratio. The H-doped oxide skin of amorphous (a50:H), cubic (c50:H) and monoclinic (m50:H) structures exhibited a negative  $U$  effect (where  $U$  is the Coulomb repulsion/correlation energy; Supplementary Fig. 10). The H<sup>+</sup> doping raised the Fermi energy above the conduction band minimum, and so resulted in an n-type conductivity (Fig. 2c for m50:H; also see Supplementary Fig. 11 for c50:H). The low effective mass of the electrons in the highly delocalized conduction band results in free-electron-like carriers in both the amorphous and crystalline oxides. This was confirmed by the Hall measurement results for the H-doped MPs (Hall coefficient =  $-1.3 \times 10^{-3}$  and Hall mobility =  $\sim 9 \text{ cm}^2 \text{ V}^{-1} \text{ s}^{-1}$ ). Figure 2d compares the calculated normalized electrical conductivities ( $\sigma/\tau_0$ ) (refs <sup>38,39</sup>) for the undoped and H-doped oxides, where  $\tau_0$  denotes the constant relaxation time. The normalized conductivity of the H-doped oxides was a couple of orders larger than those of the undoped cases, regardless of its crystallinity or In-to-Ga atomic ratios (Supplementary Fig. 12). Especially, the conductivity of

m50:8H (9.08 at% H) was higher than the value of indium tin oxide (ITO). More detailed information is provided in the Supplementary Information.

We investigated the mechanical behavior of the MPs under uniaxial elongation. Figure 3a shows optical microscope (OM) and scanning electron microscope (SEM) images of the undoped MP at different strains ( $\epsilon$ ). More MP images are shown in Supplementary Fig. 13. At  $\epsilon=50\%$ , the oxide skin was not ruptured and formed wrinkles parallel to the strain direction (Supplementary Fig. 14). Oxide-skin rupturing took place at 50–100% in all the samples. The vertical bright stripes (marked by white arrows in Fig. 3a) are the new surfaces exposed after crack formation. Wrinkles were generated in the initial oxide skin (dark region) perpendicularly to the strain direction due to the compressive force in the perpendicular direction. The crack gap increased with strain, but the width of the initial oxide stripe did not change. This selective elongation of the ruptured region is attributed to the viscous nature of the LM core. Very recently, highly ductile amorphous  $\text{Al}_2\text{O}_3$  at room temperature was reported<sup>40</sup>. We performed DFT calculations for the undoped amorphous  $\text{Ga}_2\text{O}_3$  and the H-doped amorphous  $\text{Ga}_2\text{O}_3$ . We found that amorphous  $\text{Ga}_2\text{O}_3$  is softer than the amorphous  $\text{Al}_2\text{O}_3$  and that H-doping enhances the softness (Supplementary Fig. 15). The unexpected large stretchability of the undoped MP ( $\epsilon=50\%$ ) is believed to originate partially from the intrinsic ductility and complicated surface topology formed during the synthesis.

In the H-doped MPs, we could not observe the crack formation at  $\epsilon=300\%$  (Fig. 3b; more images are shown in Supplementary Fig. 16). The initial dark lines in the OM images elongated along the strain direction without disconnection, and wrinkles developed perpendicularly to the strain direction from the left to the right sides of the MP. When the strain was released to 200%, periodic wrinkles were formed in the parallel direction to the strain (Fig. 3c) and did not disappear. This elongation and wrinkle formation implies the viscoplastic nature of the H-doped oxide. The permanent wrinkle of the H-doped MPs was also found in the printed MPs stretched at  $\epsilon=500\%$  (Fig. 3d) and after released to  $\epsilon=200\%$  (Fig. 3e). Additional wrinkles were not created during 1,000 stretching cycles. Comparatively, the undoped MPs were ruptured and the core LM leaked out at  $\epsilon=100\%$  (Supplementary Fig. 17). Figure 3f shows a control experiment with an undoped MP with PEVA adsorbed at the surface (Methods). When the MP was stretched at  $\epsilon=300\%$ , microcracks formed perpendicularly to the strain direction and wrinkles developed from the left to the right sides of the MP (more images in Supplementary Fig. 18). This result implies that the adsorbed polymer made the oxide layer ductile. On this basis, the viscoplasticity of the H-doped oxide is considered to originate from the enhanced ductility of the oxide skin by H-doping and to the adsorbed polymers.

We compared the rheological behaviour of the three types of MPs (undoped, H-doped and undoped with adsorbed PEVA) by applying a dynamic strain sweep ( $\gamma=0-1,000\%$ ) on randomly packed MPs in a confined geometry (Methods). The modulus of the H-doped MPs (and also of the undoped MPs with adsorbed PEVA) showed one order of magnitude less storage modulus ( $G'$ ) and loss modulus ( $G''$ ) than those of the undoped MPs (Supplementary Fig. 19). The solid-to-liquid transition ( $G'=G''$ , here oxide rupturing) occurred with a much larger strain in the H-doped MPs than in the undoped MPs. These results are in good agreement with OM and SEM observations and also with reported results<sup>41</sup>. Even though the viscoplasticity of the H-doped MPs is obvious from the experimental results, we cannot exclude the possibility of new oxide formation after the cracks are generated and undetected by OM. The surface area of the MP increased the initial area 1.75 times at  $\epsilon=300\%$  (see the calculation in Supplementary Information), which may indicate that the average oxide thickness decreased from 5 to 2.9 nm (a 3-nm-thick oxide<sup>41</sup> decreased to 1.8 nm). It is believed that such a

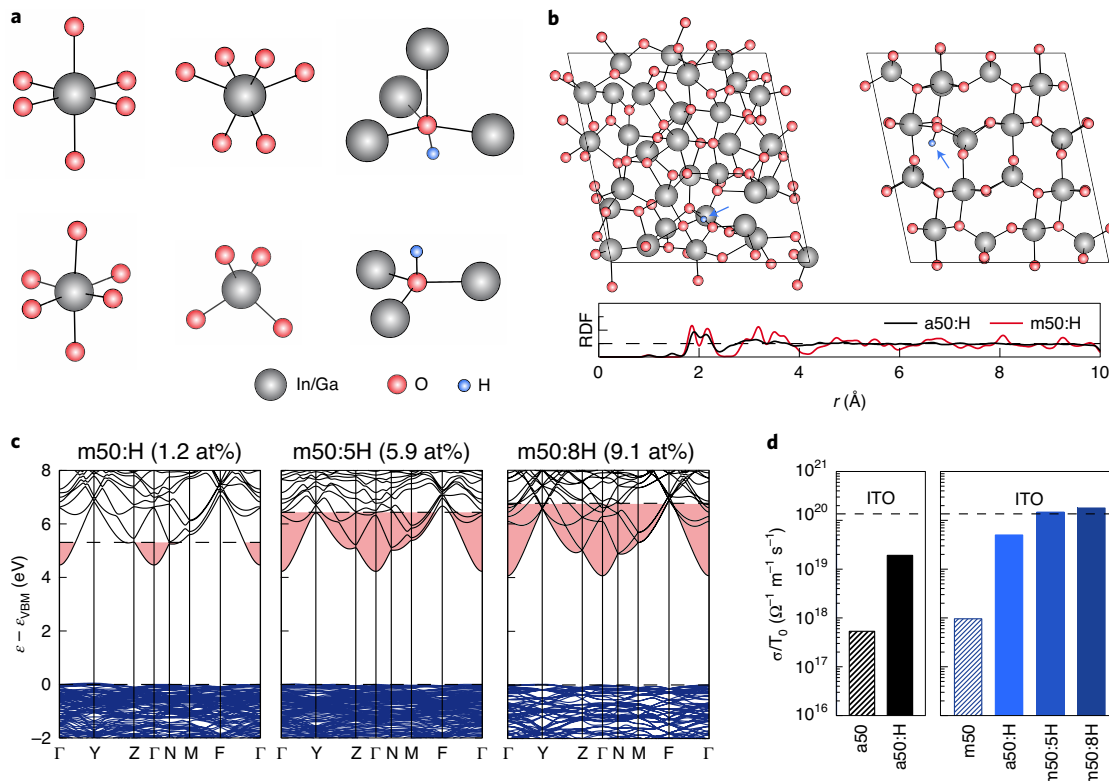


**Fig. 2 | Computational modelling of the LM oxide.** **a**, Building blocks for the cubic  $\text{In}_2\text{O}_3$  (top) and the monoclinic  $\text{Ga}_2\text{O}_3$  (bottom) crystals—two octahedral motifs for  $\text{In}_2\text{O}_3$ , and one octahedral and one tetrahedral motif for  $\text{Ga}_2\text{O}_3$ . The energetically favoured binding site of H in each oxide is shown (Supplementary Fig. 9). **b**, The atomic structures of the amorphous (a50:H (left)) and monoclinic crystalline (m50:H (right)) H-doped  $(\text{In}_{0.5}\text{Ga}_{0.5})_2\text{O}_3$  oxide. The lower panel shows the radial distribution function (RDF) plots for a50:H and m50:H. **c**, Electronic band structure of m50 with different H-doping concentrations. The valence band maximum (VBM) was set to zero, and the dashed horizontal lines denote the Fermi level. The red shaded regions denote the electron-filled conduction band. **d**, Calculated normalized electrical conductivity ( $\sigma/\tau_0$ ) of a50 (black) and m50 (blue) with different H-doping concentrations. The normalized electrical conductivity of ITO is shown for comparison. The Sn concentration in the model ITO was 2.50 at%.

solid-to-liquid transition can occur in ultrathin flawless amorphous films with a low creep activation energy<sup>42</sup>. Unfortunately, the viscous creep mechanism in amorphous oxides has been rarely investigated. A clear understanding of the large viscoplasticity observed in this study requires thorough studies on interfacial dynamics—development of a new oxidation mechanism on liquid alloys, distribution and chemical bond states of the adsorbed polymers, change of the creep activation energy by H-doping, *in situ* TEM study to monitor oxide formation under stretching and diffusion of the doped H to the newly formed oxides.

The as-synthesized H-doped LM MP solution was used as ink for nozzle printing to manufacture the circuit lines on a polydimethylsiloxane (PDMS) substrate. As the PEVA matrix strongly binds with PDMS, the printed lines were mechanically stable without peel-off under stretching. Figure 4a shows a cross-sectional SEM image of the printed line, with the densely packed MPs at the bottom. Figure 4b exhibits a top-view SEM image of the printed line obtained after etching the MPs with a concentrated HCl solution. The interconnected hollow spaces indicate that the MPs and the polymer matrix formed a bicontinuous structure in the surface region. As the oxide skin of each MP is highly conductive, the interparticle contacts maintained a good conduction in both the lateral and vertical directions. It is supposed that the electric current in the circuit line flows mainly along the bottom and then in the vertical direction, as depicted in Fig. 4c.

The diameter of the MPs was controlled by the amount of PEVA in the solution and the sonication time (Supplementary Fig. 20).

The relatively small MPs (<3 μm) were spherical without wrinkles. MPs larger than 5 μm were typically non-spherical with wrinkles (Supplementary Fig. 21) and they were located at the bottom of the printed lines. The conductivity of the circuit line increased with the size of the MPs at the same volume fraction of MPs ( $\phi_{MP} = V_{MP}/(V_{MP} + V_{polymer})$ ) (Fig. 4d) because the contact area between the MPs increased and the number of the contacts along the current path decreased. The maximum conductivity (25,000 S cm<sup>-1</sup>) was obtained with MPs of 15 μm in diameter at  $\phi_{MP} = 20\text{--}30\%$ .

Owing to the reversible elongation and retraction of the H-doped MPs on the PDMS substrate, the contact area between the MPs of the printed line reversibly increased and decreased in the low strain range (illustrated in the inset of Fig. 4e), and hence the printed line showed a reversible negative resistance change under uniaxial stretching (Fig. 4e). The resistance reduction approached saturation when  $\epsilon = 100\%$ . Figure 4f shows the negligible resistance change of the printed line during repeated stretching–releasing cycles at  $\epsilon = 500\%$ . The inset is a magnification after 1,000 stretching cycles, and exhibits identical resistance profiles between 2.9 Ω at  $\epsilon = 500\%$  and 2.4 Ω at  $\epsilon = 0\%$ . When a light emitting diode (LED) was fixed between two circuit lines, the luminance remained the same up to  $\epsilon = 500\%$  (Supplementary Fig. 22). Recently, electrical self-healing has attracted interest to implement resilient circuit lines<sup>18,43</sup>. However, the key requirement of deformable electronics is a difficult-to-cut (die-hard) electrical connection rather than healing of the disconnected line. We investigated the die-hard electrical connection by cutting the circuit line with a sharp razor blade

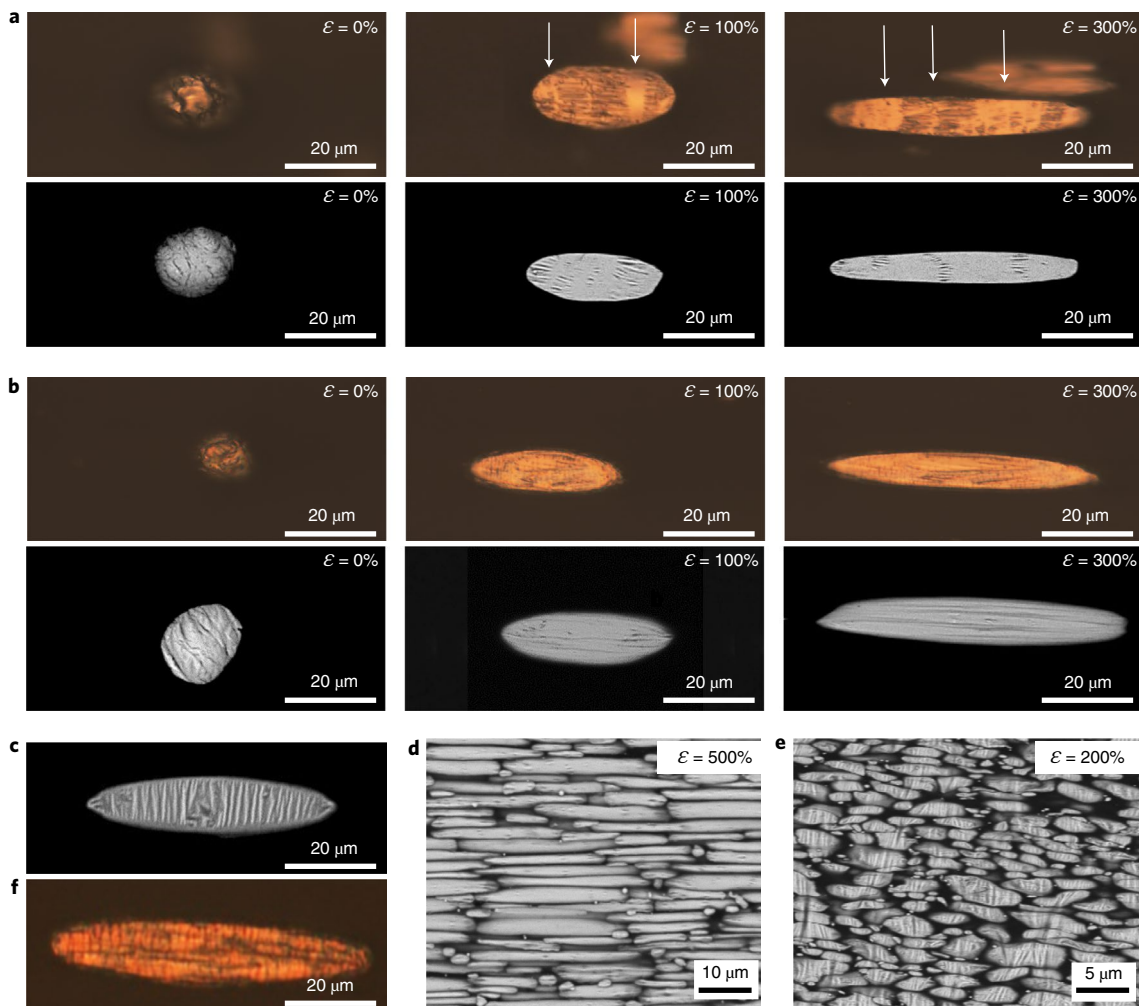


**Fig. 3 | Viscoplastic deformability of the H-doped oxide skin.** **a**, OM (top) and SEM (bottom) images of the undoped MP under uniaxial stretching. The oxide skin was ruptured, new surfaces were exposed at  $\varepsilon=100\%$  (indicated by white arrows), and the new surface selectively extended as the strain increased. Wrinkles were formed in the initial oxide skin perpendicularly to the strain direction. **b**, OM (top) and SEM (bottom) images of the H-doped MP under uniaxial stretching. No crack was found. Wrinkles were formed parallel to the strain direction (horizontal here). **c**, SEM image of the H-doped MP obtained after releasing the strain from 300 to 200%. Wrinkles were formed perpendicularly to the compressive force. **d,e**, SEM images of the printed line under uniaxial strain at  $\varepsilon=500\%$  (**d**) and after releasing the strain to  $\varepsilon=200\%$  (**e**). The oxide skin formed wrinkles after releasing the strain. **f**, OM image of the undoped MP with PEVA attached at the oxide surface when the MP was stretched at  $\varepsilon=300\%$ . Microcracks were formed instead of being ruptured and wrinkles were formed parallel to the strain direction.

(Fig. 4g) and a blunt tweezer (Fig. 4h). The light intensity of an LED connected to the lines remained unchanged during the repeated cuts (Supplementary Video 1). The cross-sectional SEM image of the printed line (Fig. 4g) taken after the razor cut exhibits that the MPs maintained their particle shape without rupturing of the oxide skin. Figure 4h shows the resistance change while simultaneously applying blunt cuts and stretching ( $\varepsilon=100\%$ ) (Supplementary Video 2). The oxide skin was ruptured by the blunt cuts and the core LM leaked out to form a continuous line.

Adjusting the concentration of PEVA in the MP ink provides options for a three-dimensional (3D) electrical connection: permanent connection, pressure-triggered connection and self-passivation. At  $\phi_{MP}=28\%$  (ink 1), the thickness of the passivation layer on the top surface was less than 1  $\mu\text{m}$  (Fig. 5a). When an additional circuit line was printed across the first line, the passivation layer blocked electrical conduction between the two lines, but the electrical connection was triggered by an external force (5 N) applied to the cross-sectional area ( $0.25 \text{ mm}^2$ ). The calculated maximum Tresca's equivalent stress ( $\sigma_{\max}$ ) of the LM oxide skin was

4.5 GPa (ref. 44). The calculated stress ( $\sigma$ ) of the oxide skin was 5 GPa by the spherical vesicle pressure model,  $\sigma=PD/(4t)$ , where  $P$  is the internal pressure,  $D$  is the diameter of the MP (5  $\mu\text{m}$ ) and  $t$  is the oxide shell thickness (5 nm). As the calculated stress was larger than the predicted  $\sigma_{\max}$  (Supplementary Information), the oxide skin could be ruptured and the core LM leaked out to connect the two lines. At  $\phi_{MP}=20\%$  (ink 2), the thickness of the passivation layer was about 7  $\mu\text{m}$  (Fig. 5b), which was electrically insulating even under a large external force (>10 N) on the cross area. Figure 5c and Supplementary Video 3 demonstrate 3D interconnections without any electrical cross-talk between the circuit lines. Line 1 corresponded to the pressure-triggered connection, and lines 2 and 3 were pressure insensitive. When voltage (3 V) was applied to either line 1 or 3 (Fig. 5c(i),(ii)), LED A or C, respectively, turned on. When the cross-regions between lines 1 and 2 (marked by violet boxes) were pressed while the voltage was applied to line 1, LED B turned on (Fig. 5c(iii)). Meanwhile, pressing the cross-over between lines 2 and 3 did not turn on LED C due to the thick passivation layer of line 2 (Fig. 5c(iv)).

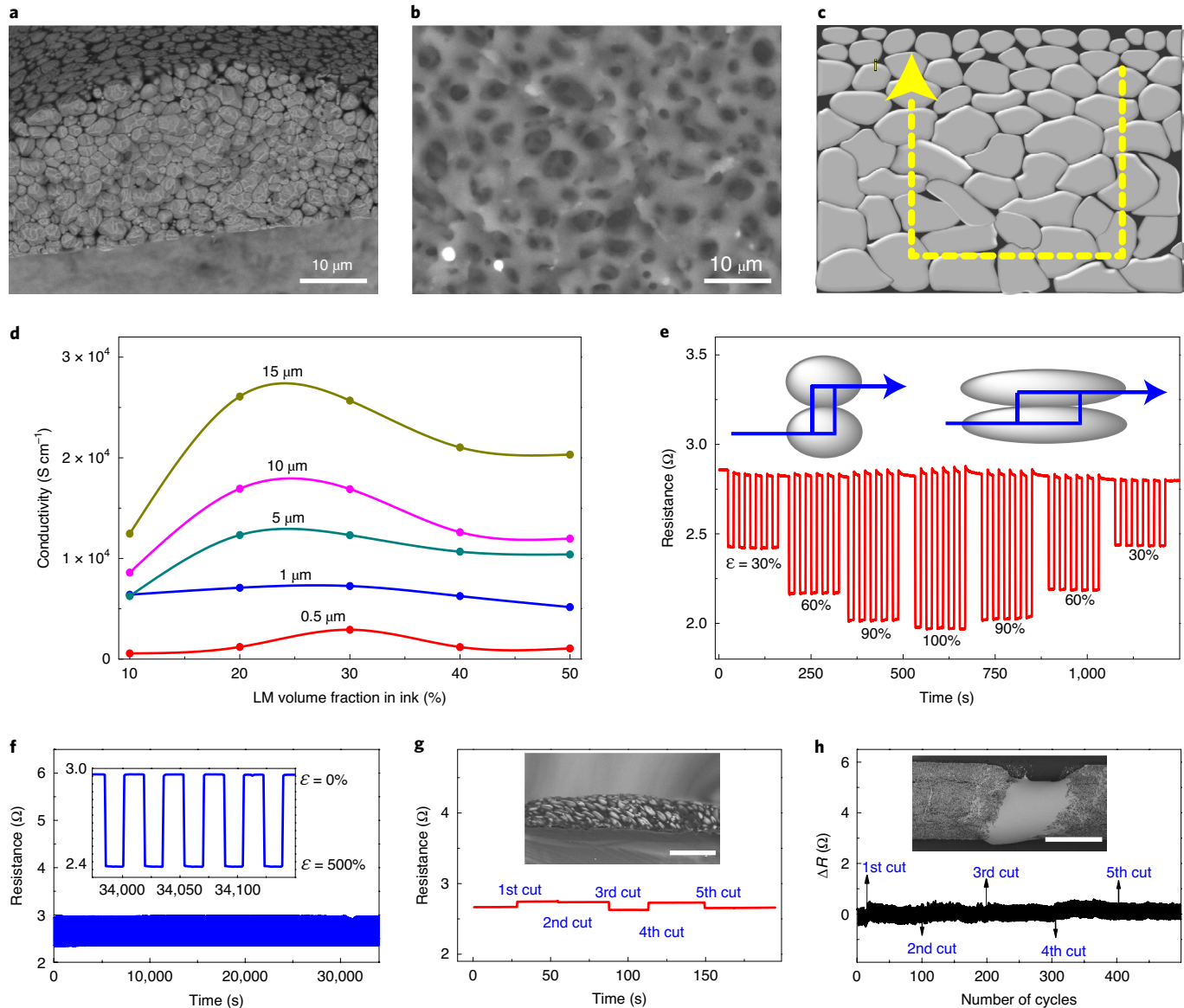


**Fig. 4 | Electrical and mechanical stability of the printed LM MP circuit line.** **a**, Cross-sectional SEM image of the printed circuit line prepared with PEVA ( $\phi_E = 0.88$ ). **b**, Top-view SEM image of the printed line after etching the MPs with HCl. **c**, Schematic of the electrical conduction path. **d**, Change of the conductivity of the circuit line as a function of the LM volume fraction (10, 20, 30, 40 and 50%). The average diameter of the LM MPs varied (0.5, 1, 5, 10 and 15  $\mu\text{m}$ ). **e**, Resistance decrease of the printed H-doped MPs under repeated uniaxial stretching. Inset: increase in the contact area between the MPs by the elongation under stretching. **f**, Resistance of the circuit line during 1,000 cyclic stretches at  $\varepsilon = 500\%$ . Inset: magnification of the resistance after 1,000 stretching cycles. **g**, Resistance of the circuit line during repeated razor-blade sharp cuts. Inset: cross-sectional SEM image after a sharp cut. Scale bar, 50  $\mu\text{m}$ . **h**, Resistance change of the circuit line while simultaneously repeating the stretch ( $\varepsilon = 100\%$ ) and repeated blunt cuts with a large tweezer. Inset: SEM image after the test. Scale bar, 250  $\mu\text{m}$ .

The passivated line showed excellent electrical stability under thermal and moisture environments. The resistance of the circuit line at 100 °C showed no difference for 12 weeks (Fig. 5d), which indicates no further oxidation at high temperature. The resistance at -20 °C was slightly high and stabilized after four weeks, which shows that Joule heating during measurements improved the contacts between MPs. The passivated circuit line showed no resistance change in 90% humidity at 40 °C for the entire period (30 days) (Fig. 5e), whereas the non-passivated line was stable for initial 4 days but lost conductivity after 20 days.

The self-passivation enabled direct printing of multilayer coils. Figure 5f illustrates a double-layer planar coil printed with the self-passivation ink (ink 2). The bottom coil was printed in the

anticlockwise direction, and the centre of the coil was scratched to leak the LM, and then the top coil was printed starting from the centre in the clockwise direction. The width, height and space of the coil were 500, 90 and 250  $\mu\text{m}$ , respectively (Fig. 5g and Supplementary Fig. 23). The double-layer coil was highly stretchable with negligible resistance changes (Supplementary Fig. 24). The double-layer coil had a high inductance (4.25  $\mu\text{H}$ ) at 100 kHz, which is much higher than the reported values of the stretchable coils made of the serpentine structure (~100 nH) (ref. <sup>45</sup>) and of the LM microchannel (0.712  $\mu\text{H}$ ) (ref. <sup>46</sup>). The inductive coil sensor showed excellent repeatability and negligible standard deviations, regardless of the strain, up to  $\varepsilon = 100\%$  (Fig. 5h). As the coil resistance was unchanged by deformation, the inductance was

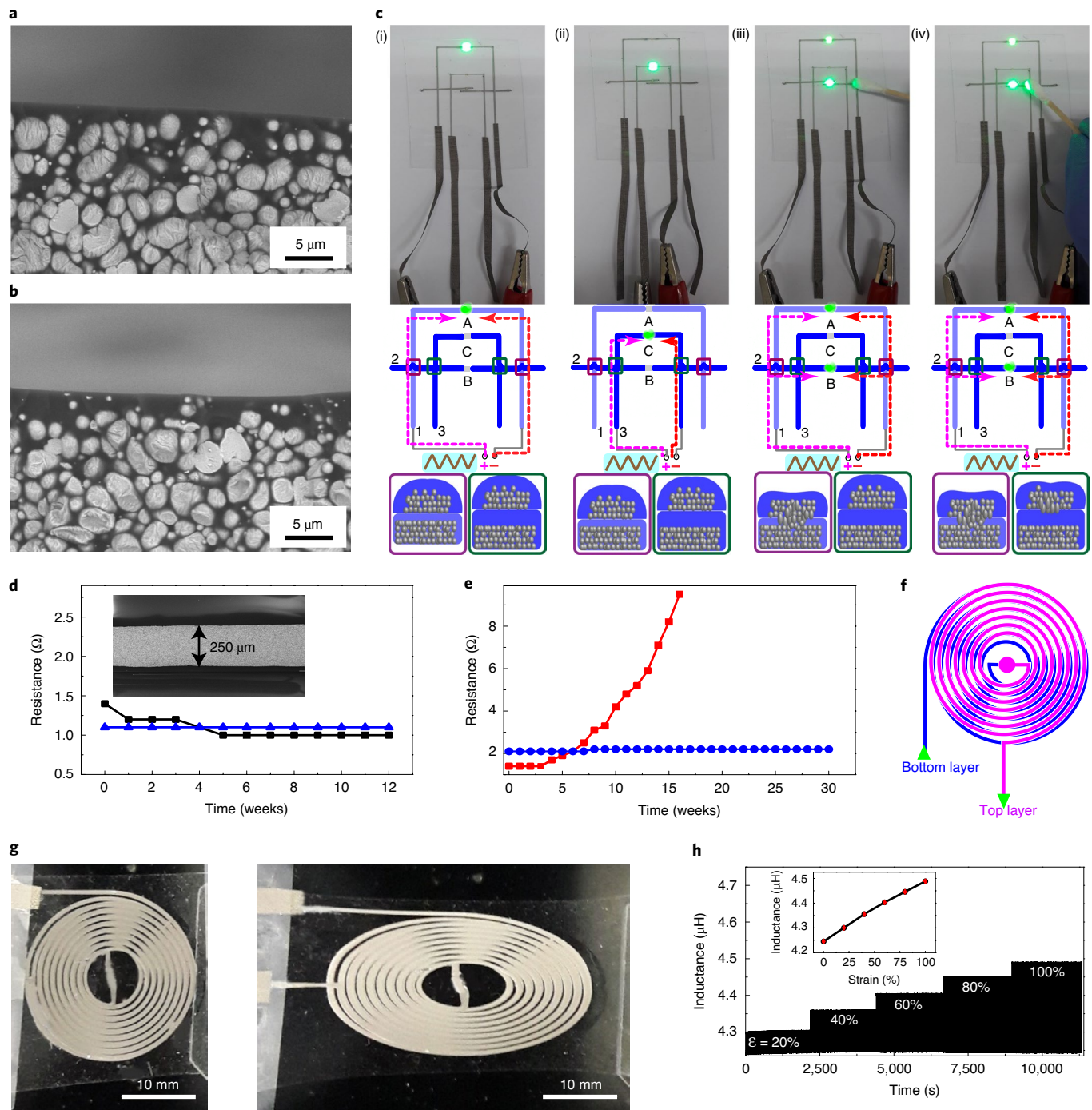


**Fig. 5 | Printed 3D circuit line with autonomous self-passivation.** **a,b**, Cross-section SEM images of the printed circuit line with a thin passivation layer (line 1 in **c**) (**a**) and a thick passivation layer (lines 2 and 3 in **c**) (**b**). **c**, Digital images (top) and schematic (middle) of the circuit lines 1, 2 and 3, and cross-sectional schemes (bottom) of lines 1 and 2 (left, violet box) and lines 2 and 3 (right, green box). **i,ii**, LED A or LED C turned on when the voltage was applied. **iii**, LED B turned on when pressure was applied at the cross-over between lines 1 and 2. **iv**, LED C did not turn on when pressure was applied at the cross-over between lines 2 and 3. The arrows in the scheme denote the electric current. **d**, Resistance of the circuit line at  $T = -20^{\circ}\text{C}$  (black) and  $100^{\circ}\text{C}$  (red). Inset: SEM image of the circuit line. **e**, The resistance of the circuit line with (blue) and without (red) the passivation layer tested for 30 days at 90% humidity and  $T = 40^{\circ}\text{C}$ . **f**, Scheme of the double-layer planar coil. **g**, Digital images of the double-layer coil at  $\epsilon = 0\%$  (left) and 100% (right). **h**, Change of the inductance during the repeated uniaxial stretching test at various strains. Inset: inductance versus strain graph.

governed by the area of the coil, and thus it had a linear response to strains.

In summary, we have revealed that excessive hydrogen doping in  $\text{Ga}_x\text{In}_{2-x}\text{O}_3$  filled the electronic band structure and resulted in a high electrical conductivity comparable to that of the ITO electrode. We also found that H-doping and polymer adsorption to the LM oxide

surface synergistically made the oxide viscoplastic, and thus the H-doped MPs were deformable without crack formation in the oxide skin. The printed circuit line with ink that consisted of the H-doped MPs and polymer had a conductivity similar to that of the bulk LM. The circuit lines showed negligible resistance change up to a 500% elongation strain and maintained the same conductivity

under repeated mechanical cuts in wide ranges of temperature and humidity. Owing to the self-passivation of the printing, complex 3D circuits could be printed and double-layer planar coils could be fabricated for use as an inductive stretchable strain sensor.

## Online content

Any methods, additional references, Nature Research reporting summaries, source data, extended data, supplementary information, acknowledgements, peer review information; details of author contributions and competing interests; and statements of data and code availability are available at <https://doi.org/10.1038/s41563-020-00863-7>.

Received: 15 September 2019; Accepted: 23 October 2020;  
Published online: 04 January 2021

## References

- Gao, W. et al. Fully integrated wearable sensor arrays for multiplexed in situ perspiration analysis. *Nature* **529**, 509–514 (2016).
- You, I. et al. Stretchable E-skin apexcardiogram sensor. *Adv. Mater.* **28**, 6359–6364 (2016).
- Xu, S., Jayaraman, A. & Rogers, J. A. Skin sensors are the future of health care. *Nature* **571**, 319–321 (2019).
- Wang, S., Oh, J. Y., Xu, J., Tran, H. & Bao, Z. Skin-inspired electronics: an emerging paradigm. *Acc. Chem. Res.* **51**, 1033–1045 (2018).
- Chortos, A., Liu, J. & Bao, Z. Pursuing prosthetic electronic skin. *Nat. Mater.* **15**, 937–950 (2016).
- Yu, X. et al. Skin-integrated wireless haptic interfaces for virtual and augmented reality. *Nature* **575**, 473–479 (2019).
- Dickey, M. D. Stretchable and soft electronics using liquid metals. *Adv. Mater.* **29**, 1606425 (2017).
- Chu, K. et al. Smart passivation materials with a liquid metal microcapsule as self-healing conductors for sustainable and flexible perovskite solar cells. *Adv. Funct. Mater.* **28**, 1800110 (2018).
- Roh, H. et al. Liquid metal covered with thermoplastic conductive composites for high electrical stability and negligible electromechanical coupling at large strains. *ACS Appl. Mater. Interfaces* **11**, 26204–26212 (2019).
- Kim, H. W. et al. Hygroscopic auxetic on-skin sensors for easy-to-handle repeated daily use. *ACS Appl. Mater. Interfaces* **10**, 40141–40148 (2018).
- Song, J. H. et al. Surface-embedded stretchable electrodes by direct printing and their uses to fabricate ultrathin vibration sensors and circuits for 3D structures. *Adv. Mater.* **29**, 1702625 (2017).
- Choi, S., Han, S. I., Kim, D., Hyeon, T. & Kim, D. H. High-performance stretchable conductive nanocomposites: materials, processes, and device applications. *Chem. Soc. Rev.* **48**, 1566–1595 (2019).
- Hirsch, A., Dejace, L., Michaud, H. O. & Lacour, S. P. Harnessing the rheological properties of liquid metals to shape soft electronic conductors for wearable applications. *Acc. Chem. Res.* **52**, 534–544 (2019).
- Daeneke, T. et al. Liquid metals: fundamentals and applications in chemistry. *Chem. Soc. Rev.* **47**, 4073–4111 (2018).
- Boley, J. W., White, E. L. & Kramer, R. K. Mechanically sintered gallium–indium nanoparticles. *Adv. Mater.* **27**, 2355–2360 (2015).
- Wang, J. X. et al. Printable superelastic conductors with extreme stretchability and robust cycling endurance enabled by liquid–metal particles. *Adv. Mater.* **30**, 1706157 (2018).
- Xin, Y. M., Peng, H., Xu, J. & Zhang, J. Y. Ultrauniform embedded liquid metal in sulfur polymers for recyclable, conductive, and self-healable materials. *Adv. Funct. Mater.* **29**, 1808989 (2019).
- Markvicka, E. J., Bartlett, M. D., Huang, X. N. & Majidi, C. An autonomously electrically self-healing liquid metal–elastomer composite for robust soft-matter robotics and electronics. *Nat. Mater.* **17**, 618–624 (2018).
- Zhu, S. et al. Ultrastretchable fibers with metallic conductivity using a liquid metal alloy core. *Adv. Funct. Mater.* **23**, 2308–2314 (2013).
- Guo, R., Sun, X. Y., Yuan, B., Wang, H. Z. & Liu, J. Magnetic liquid metal (Fe–EGaIn) based multifunctional electronics for remote self-healing materials, degradable electronics, and thermal transfer printing. *Adv. Sci.* **6**, 1901478 (2019).
- Wang, X. L. et al. Soft and moldable Mg-doped liquid metal for conformable skin tumor photothermal therapy. *Adv. Healthc. Mater.* **7**, 1800318 (2018).
- Tang, J. B. et al. Gallium-based liquid metal amalgams: transitional-state metallic mixtures (TransM<sup>ixes</sup>) with enhanced and tunable electrical, thermal, and mechanical properties. *ACS Appl. Mater. Interfaces* **9**, 35977–35987 (2017).
- Zheng, R. M. et al. A novel conductive core–shell particle based on liquid metal for fabricating real-time self-repairing flexible circuits. *Adv. Funct. Mater.* **30**, 1910524 (2020).
- Çınar, S., Tevis, I. D., Chen, J. & Thuo, M. Mechanical fracturing of core–shell undercooled metal particles for heat-free soldering. *Sci. Rep.* **6**, 21864 (2016).
- Desai, V., Shenoy, M. A. & Gogate, P. R. Ultrasonic degradation of low-density polyethylene. *Chem. Eng. Process.* **47**, 1451–1455 (2008).
- Liu, S. Q., Gong, W. G. & Zheng, B. C. The effect of peroxide cross-linking on the properties of low-density polyethylene. *J. Macromol. Sci. B* **53**, 67–77 (2014).
- Suslick, K. S., Gawienowski, J. J., Schubert, P. F. & Wang, H. H. Alkane sonochemistry. *J. Phys. Chem.* **87**, 2299–2301 (1983).
- Kim, M. H. et al. Photochemical hydrogen doping induced embedded two-dimensional metallic channel formation in InGaZnO at room temperature. *ACS Nano* **9**, 9964–9973 (2015).
- Cademartiri, L. et al. Electrical resistance of Ag<sup>TS</sup>–S(CH<sub>2</sub>)<sub>n</sub>–CH<sub>3</sub>//Ga<sub>2</sub>O<sub>3</sub>/EGaIn tunneling junctions. *J. Phys. Chem. C* **116**, 10848–10860 (2012).
- Zhang, C. et al. Plasma treatment of ITO cathode to fabricate free electron selective layer in inverted polymer solar cells. *J. Mater. Chem. C* **2**, 8715–8722 (2014).
- Huang, C. J. et al. Effect of OH<sup>-</sup> on chemical mechanical polishing of β-Ga<sub>2</sub>O<sub>3</sub>(100) substrate using an alkaline slurry. *RSC Adv.* **8**, 6544–6550 (2018).
- Surdu-Bob, C. C., Saeid, S. O. & Sullivan, J. L. An X-ray photoelectron spectroscopy study of the oxides of GaAs. *Appl. Surf. Sci.* **183**, 126–136 (2001).
- Donley, C. et al. Characterization of indium–tin oxide interfaces using X-ray photoelectron spectroscopy and redox processes of a chemisorbed probe molecule: effect of surface pretreatment conditions. *Langmuir* **18**, 450–457 (2002).
- Yong, Y. Q. et al. Use of decomposable polymer-coated submicron Cu particles with effective additive for production of highly conductive Cu films at low sintering temperature. *J. Mater. Chem. C* **5**, 1033–1041 (2017).
- Wei, Y. D. et al. Interaction between hydrogen and gallium vacancies in β-Ga<sub>2</sub>O<sub>3</sub>. *Sci. Rep.* **8**, 10142 (2018).
- Wu, Y. Z. et al. Atomic layer deposition of In<sub>2</sub>O<sub>3</sub>H from InCp and H<sub>2</sub>O/O<sub>2</sub>: microstructure and isotope labeling studies. *ACS Appl. Mater. Interfaces* **9**, 592–601 (2017).
- Sheng, J., Park, E. J., Shong, B. & Park, J. S. Atomic layer deposition of an indium gallium oxide thin film for thin-film transistor applications. *ACS Appl. Mater. Interfaces* **9**, 23934–23940 (2017).
- Madsen, G. K. H. & Singh, D. J. BoltzTraP: A code for calculating band-structure dependent quantities. *Comput. Phys. Commun.* **175**, 67–71 (2006).
- Jang, W., Lee, J., In, C., Choi, H. & Soon, A. Designing two-dimensional Dirac heterointerfaces of few-layer graphene and tetradymite-type Sb<sub>2</sub>Te<sub>3</sub> for thermoelectric applications. *ACS Appl. Mater. Interfaces* **9**, 42050–42057 (2017).
- Frankberg, E. J. et al. Highly ductile amorphous oxide at room temperature and high strain rate. *Science* **366**, 864–869 (2019).
- Jacob, A. R., Parekh, D. P., Dickey, M. D. & Hsiao, L. C. Interfacial rheology of gallium-based liquid metals. *Langmuir* **35**, 11774–11783 (2019).
- Fehlner, F. P. & Mott, N. F. Low-temperature oxidation. *Oxid. Met.* **2**, 59–99 (1970).
- Oh, J. Y., Kim, S., Baik, H. K. & Jeong, U. Conducting polymer dough for deformable electronics. *Adv. Mater.* **28**, 4455–4461 (2016).
- Tang, L. et al. Printable metal–polymer conductors for highly stretchable bio-devices. *iScience* **4**, 302–311 (2018).
- Lazarus, N., Meyer, C. D. & Bedair, S. S. Stretchable inductor design. *IEEE Trans. Electron Dev.* **62**, 2270–2277 (2015).
- Fassler, A. & Majidi, C. Soft-matter capacitors and inductors for hyperelastic strain sensing and stretchable electronics. *Smart Mater. Struct.* **22**, 055023 (2013).

**Publisher's note** Springer Nature remains neutral with regard to jurisdictional claims in published maps and institutional affiliations.

© The Author(s), under exclusive licence to Springer Nature Limited 2021

## Methods

**Preparation of LM MPs ink.** PEVA (0.2 g) and DCP (4 mg) were dissolved in toluene (5 ml). Different amounts of bulk LM (0.07, 0.14, 0.32, 0.56, 0.86 and 1.30 g) were introduced to the toluene solution, which corresponded to 5, 10, 20, 30, 40 and 50 vol% versus PEVA. MPs were prepared by ultrasonication of the toluene solution for 15 min with a Sonics Vibra CV334 (13 mm tip). The solution temperature reached up to 98 °C during ultrasonication. The as-sonicated solution was used as the ink for printing. THF was used as a solvent to prepare the ink for FR and PU.

**Preparation of the undoped MP with adsorbed PEVA.** We prepared the undoped MPs in pure toluene. We added the same amount of PEVA and DCP for the H-doped MPs in the as-prepared undoped MP solution. The solution was heated at 150 °C for 1 h under mechanical stirring. The resultant MPs were suspended for 30 min due to the attachment of the polymer, as observed in the H-doped MPs. The MPs were not conductive. For the observation of mechanical deformation of the MP, we washed the MP with pure toluene with five cycles of centrifuge and washing.

**Fabrication of the circuit lines.** The MP ink was printed with a nozzle printer (Musashi, Image Master 350PC) on the PDMS substrate. The nozzle diameter was 100 μm and the dispensing pressure varied from 50 to 100 kPa to control the width of the printed lines. After printing, the specimen was annealed at 120 °C for 3 h to remove the solvent and to create the passivation layer. For the light intensity measurements, LEDs were placed to bridge two circuit lines and annealed at 120 °C for 1 h. Constant current (100 μA) was applied with Keithley 2400. For the 3D interconnection, the first line (ink 1) was printed on the PDMS substrate and annealed at 120 °C for 3 h. The second line (ink 2) was printed over the first line and annealed at 120 °C for 3 h. The third line (ink 2) was printed over the second line, parallel to the first line. LEDs were embedded in the middle of the lines. For the fabrication of the double-layer induction coil, the bottom coil was printed on the PDMS substrate using ink 2 in an anticlockwise direction and annealed at 100 °C for 3 h in the printing stage to create the passivation layer. The centre point of the coil was damaged with a tweezer to let the LM squeeze out from the passivation layer. The top coil was printed, starting from the centre in a clockwise direction and annealed at 100 °C for 3 h.

**Electrical measurement and characterization.** The electrical conductivity was measured using the equation,  $\sigma = I / V W h$ , where  $V$  is the voltage,  $W$  is width (cm),  $h$  is the height (h),  $I$  is the current (A),  $l$  is the measurement distance (cm) and  $\sigma$  is the conductivity ( $S \text{ cm}^{-1}$ ). The  $I$ - $V$  characteristics were measured by a semiconductor parameter analyser (Agilent 4156A) and Keithley 2400 source meter. The resistance change under uniaxial stretching was measured using a universal measurement probe (UMP 100, Teraleader Co.). The inductance of the sensor was measured at 100 kHz and 0.5 V using a LCR meter (E-880AL, Keysight). The morphology of the circuit line was analysed using SEM (HITACHI TM-1000, Tabletop microscope), OM (Olympus BX-51), field-emission SEM (S-00, Hitachi) and scanning transmission electron microscope (JEM-2100F) at an accelerating voltage of 200 kV. XPS measurements were carried out in a K-Alpha (Thermo VG) equipped with monochromated Al X-ray sources (Al K $\alpha$  line, 1,486.6 eV run at 12 kV and 3 mA, with a fixed analyser transmission). The peaks were deconvoluted using the Gaussian–Lorentzian method. Atomic fraction (at%) was calculated using the equation,  $\text{at\%} = [(A_{\text{at}}/S_{\text{at}})/\sum(A_{\text{at}}/S_{\text{at}})] \times 100$ , where  $A_{\text{at}}$  is the peak area and  $S_{\text{at}}$  is the sensitivity factor of the peak. X-ray diffraction (RIGAKU/MAX-2500/PC) with Cu K $\alpha$  radiation ( $\lambda = 0.1542 \text{ nm}$ ). Details of the APT measurements are provided in the Supplementary Information.

**Rheological measurements.** The rheology test was performed at 25 °C with a rotational rheometer having a two-parallel-plate geometry (Anton Paar). The diameter of the top plate was 40 mm. The bottom plate was cup-shaped to prevent flow of the LM. A dilute MP suspension was dropped into and evaporated in the bottom plate. We performed the same MP deposition process repeatedly to prepare a densely packed MP multilayer. The thickness of the multilayer was fixed to be

500 μm and the average size of the MPs was ~3 μm for all the types of the MPs. A dynamic strain sweep was carried out at a fixed frequency of 0.2 rad s $^{-1}$  and the strain amplitude was varied from 0.1 to 1,000%.

**DFT calculations.** All first-principles DFT calculations were performed using the Vienna Ab-initio Simulation Package<sup>47</sup> with the PBEsol exchange correlation functional<sup>48</sup>. To model the amorphous systems, we performed ab initio molecular dynamics calculations by adapting the heat-and-quench method. The normalized electrical conductivities in this work were then calculated by solving the Boltzmann transport equation within the constant relaxation time approximation, as implemented in the BoltzTraP code<sup>38</sup>.

## Data availability

All the data that support this study are included in this article and its supplementary information files. Source data are provided with this paper.

## References

47. Kresse, G. & Furthmüller, J. Efficient iterative schemes for ab initio total-energy calculations using a plane-wave basis set. *Phys. Rev. B* **54**, 11169–11186 (1996).
48. Perdew, J. P. et al. Restoring the density-gradient expansion for exchange in solids and surfaces. *Phys. Rev. Lett.* **100**, 136406 (2008).

## Acknowledgements

S.V. and U.J. acknowledge the support of a National Research Foundation of Korea (NRF) grant funded by the Korea government (MSIT) (no. NRF-2020R1A2C3012738), the Center for Advanced Soft-Electronics funded by the Ministry of Science, ICT and Future Planning as Global Frontier Project (CASE-2015M3A6A5072945) and the Korea Research Institute of Chemical Technology (KRICT). W.J., E.K. and A.S. gratefully acknowledge support from the Ministry of Science and ICT under the Creative Materials Discovery Program (2018M3D1A1058536) and computational resources from KISTI (KSC-2019-CRE-0024). H.W. and L.B. are thankful for the financial support of a Marie Skłodowska-Curie Individual Fellowship ('3D-SITS') from the European Union's Horizon 2020 research and innovation programme (no. 799733). J.B.S. appreciates financial support from the Ministry of Science and ICT (MSIT) of the Korean government (no. 2018R1C1B6008585). The authors thank S. J. Park and J. M. Park (POSTECH) for supporting the rheology measurements.

## Author contributions

S.V., H.W., L.B. and U.J. designed the experiment. S.V. carried out the fabrication and characterization of the LM MP circuit lines, analysed the data and wrote the manuscript along with U.J. A.S., W.J. and M.E.K. designed the theoretical part and wrote the corresponding part of the manuscript. J.B.S. performed the APT analysis. K.T., G.P. and I.Y. performed the electrical characterization of the conductive LM MPs and assisted the characterization of the die-hard properties of the circuit line. M.K., J.K., G.L., W.S. and A.G. assisted the characterization of the LM MP circuits.

## Competing interests

Patent applications (Korean Patent application numbers 10-2020-0038722 and 10-2020-0033237) have been filed based on the results of this study.

## Additional information

**Supplementary information** is available for this paper at <https://doi.org/10.1038/s41563-020-00863-7>.

**Correspondence and requests for materials** should be addressed to A.S. or U.J.

**Peer review information** *Nature Materials* thanks Michael Dickey and the other, anonymous, reviewer(s) for their contribution to the peer review of this work.

**Reprints and permissions information** is available at [www.nature.com/reprints](http://www.nature.com/reprints).